Over 12% efficient kesterite solar cell via back interface engineering

Y. Zhao, Z Yu, J. Hu, Z Zheng, H. Ma, K. Sun, X. Hao, G. Liang, P. Fan, Xianghua Zhang, et al.

Over 12% efficient kesterite solar cell via back interface engineering

YunHai Zhao[a,b], ZiXuan Yu[a], JuGuang Hu[a], ZhuangHao Zheng[a], HongLi Ma[b], Kaiwen Sun[c], XiaoJing Hao[c], GuangXing Liang[a,*], Ping Fan[a,d,*], XiangHua Zhang[b], ZhengHua Su[a,*]

[a.]Shenzhen Key Laboratory of Advanced Thin Films and Applications, Key Laboratory of Optoelectronic Devices and Systems, College of Physics and Optoelectronic Engineering, Shenzhen University, Shenzhen 518060, Guangdong, China

[b.]CNRS, ISCR (Institut des Sciences Chimiques de Rennes) UMR 6226, Univ Rennes, Rennes, F–35000, France

[c.]School of Photovoltaic and Renewable Energy Engineering, UNSW Sydney, Sydney, NSW 2052, Australia

[d.]Shenzhen University Institute of Microscale Optoelectronics, Shenzhen University, Shenzhen 518060, Guangdong, China

∗ Corresponding authors.

E–mail addresses: zhsu@szu.edu.cn (Z.H. Su), lgx@szu.edu.cn (G.X. Liang); fanping@szu.edu.cn (P. Fan)

Abstract

Kesterite $Cu_2ZnSn(S,Se)_4$ (CZTSSe) has attracted considerable attention as a non–toxic and earth–abundant solar cell material. During selenization of CZTSSe film at high temperature, the reaction between CZTSSe and Mo is one of the main reasons that result in unfavorable absorber and interface quality, which leads to large open circuit voltage deficit ($V_{OC–def}$) and low fill factor (FF). Herein, a WO_3 intermediate layer introduced at the back interface can effectually inhibit the unfavorable interface reaction between absorber and back electrode in the preliminary selenization progress; thus high–quality crystals are obtained. Through this

back interface engineering, the traditional problems of phase segregation, voids in the absorber and over thick $Mo(S,Se)_2$ at the back interface can be well solved, which greatly lessens the recombination in the bulk and at the interface. The increased minority carrier diffusion length, decreased barrier height at back interface contact and reduced deep acceptor defects give rise to systematic improvement in V_{OC} and FF, finally a 12.66% conversion efficiency for CZTSSe solar cell has been achieved. This work provides a simple way to fabricate highly efficient solar cells and promotes a deeper understanding of the function of intermediate layer at back interface in kesterite-based solar cells.

Keywords: $Cu_2ZnSn(S,Se)_4$; WO_3 intermediate layer; Crystal growth; Minority carrier diffusion length; Interface contact quality.

1. Introduction

The kesterite $Cu_2ZnSn(S,Se)_4$ (CZTSSe) thin film solar cells have attracted considerable interest as potential alternatives for the high–efficiency solar devices such as $Cu(In,Ga)Se_2$ (CIGS) and CdTe thin-film solar cells. This material family enjoys its compelling features of optimal band gap (E_g), remarkable absorption coefficients ($>10^4$ cm^{-1}), abundant and nontoxic elements, and thermodynamically stable structure [1–3]. However, the highest CZTSSe solar cell efficiency is only 13.5% up to now, which is stagnated compared to those of CIGS (23.35%) and CdTe (22.1%) [4]. The major bottleneck restricting the development of kesterite–based CZTSSe is the large open–circuit voltage deficit (V_{OC-def}) and the low fill factor (FF), which mainly attributes to the unfavorable absorber and interface quality [5–7]. Back interface engineering is one of the important directions to obtain absorber and interface with high quality. This is because the poor back interface leads to decomposition reactions, which form secondary phases and voids that seriously deteriorate the quality of the absorber and interface [8,9].

Thermodynamic calculations show that CZTSSe readily decomposes into secondary phase [such as Zn(S,Se), Sn(S,Se) and $Cu_2(S,Se)$] and forms thick $Mo(S,Se)_2$ layers and voids during the selenization at high temperature [10,11].

$$Cu_2ZnSn(S,Se)_4+Mo \rightarrow Cu_2(S,Se)+Zn(S,Se)+Sn(S,Se)+Mo(S,Se)_2 \quad (1)$$

Typically, the nucleation process of CZTSSe begins at the surface due to the relatively high selenium partial pressure during selenization. However, relevant studies show that the Mo back electrode plays a vital role in inducing the bottom nucleation of absorber, so crystal growth occurs simultaneously at the surface and back interfaces. This bidirectional grain growth process results in a typical double layer structure with poor crystallinity, resulting in a short diffusion length of minority carrier in CZTSSe devices [12,13]. In addition, the over thick $Mo(S,Se)_2$ at the back interface is another serious problem commonly existing in kesterite devices prepared by spin–coating and selenization process. Too thick $Mo(S,Se)_2$ at the back interface can significantly reduce the thickness of Mo back electrode, worsen the electrical

contact between absorber and electrode, and all of this increase the series resistance (R_s) and the contact barrier height (Φ_B) at back interface [14–16]. One of the effective methods to solve the problem of poor absorber crystallization and thick $Mo(S,Se)_2$ is to introduce an intermediate layer between CZTSSe and Mo to control the harmful back interface reaction. For example, Cui et al. deposited 20 nm Ag on Mo electrode to improve CZTS/Mo contact and achieved a device efficiency of 4.42% [17]; Shin et al. used the TiN diffusion barrier and demonstrated 8.9% efficiency CZTSe solar cells with a improved carriers lifetime [18]; Meng et al. obtained 11.68% efficiency in preparing high quality CZTSSe single–layer crystals by introducing MoO_3 isolating layer [12]. By introducing WO_3 intermediate layer at back interface, Yao et al. obtained CZTSSe devices with thin $Mo(S,Se)_2$ and good absorber crystallinity, demonstrating the potential of WO_3 intermediate layer to obtain high performance CZTSSe device[19]. However, although the experimental study has proved the positive effect of the WO_3 intermediate layer on effectively inhibiting the interface decomposition reaction, the essence of the interaction between the WO_3 intermediate layer and the fundamental mechanism of efficiency improvement has not been fully revealed and needs further study. More importantly, the effect of the WO_3 intermediate layer on the grain growth mechanism of the absorber, the formation of $Mo(S,Se)_2$, the minority carriers diffusion length and the contact barrier at the back interface have not been fully studied. Hence, the effect of WO_3 intermediate layer on CZTSSe absorber needs to be re–investigated to provide guidance to improve the grain growth mechanism of CZTSSe absorber, suppress the carrier recombination of CZTSSe absorber and enhance CZTSSe device performance.

Herein, a WO_3 intermediate layer was introduced to solve the problem of poor crystallinity quality of CZTSSe absorber and the unfavorable front and back interface contact, thus the diffusion length of minority carrier is improved, and the contact barrier height is reduced. We systematically investigated the effects of WO_3 intermediate layer on the microstructure, electrical and defects property of CZTSSe for the first time. The WO_3 intermediate layer

initially prevents direct contact of CZTSSe with back electrode. Hence, the decomposition of CZTSSe and the formation of $Mo(S,Se)_2$ were inhibited, which was beneficial to obtaining good absorber crystallinity and better back contact, significantly increased the minority carriers diffusion length and reduced the back interface contact barrier height. Besides, due to the improvement of crystal growth process, the dense absorber with good crystallization has a smoother surface, which makes better contact quality of CZTSSe/CdS interface and lower interface defect density. This method not only improves interface and bulk carrier transportation, but also reduces the deep accepter defect density, resulting in suppressed non–radiative recombination. Our handy and convenient strategy achieved a CZTSSe device efficiency of 12.66% (the total–area efficiency is 12.1%) with significant reduction in V_{OC-def}. We claim that this back interface engineering provides a straightforward and economical method for manufacturing highly efficient CZTSSe devices. At the same time, this study is helpful to further understand the deep reasons for CZTSSe device efficiency improvement.

2. Experimental Section

2.1. Formation of Precursor Solutions

For Sn^{4+} precursor solution, CuCl, $Zn(CH_3COO)_2 \cdot 2H_2O$, $SnCl_4 \cdot 5H_2O$ and $SC(NH_2)_2$ were dissolved in 2–methoxyethanol, and for Sn^{2+} precursor solution, $Cu(CH_3COO)_2 \cdot H_2O$, $ZnCl_2$, $SnCl_2 \cdot 2H_2O$ and $SC(NH_2)_2$ were dissolved in 2–methoxyethanol. The precursor solutions were stirred at 60 ℃ for one hour to get a deep yellow solution. The ratio of Cu/(Zn+Sn) was 0.775 and the ratio of Zn/Sn was 1.2. Then Sn^{4+} and Sn^{2+} precursor solutions were evenly mixed 1:1 and diluted to half of the original concentration to obtain precursor solution. The detailed fabrication process for precursor solution can be seen in our previous work [15].

2.2. Device fabrication

WO_3 films with thickness of 10, 15 and 20 nm were evaporated on Mo–coated soda–lime glass substrate by using TEMD500 evaporator. CZTSSe precursor films were prepared by spin-

coating. The spin-coating step was repeated ten times with 3000 r min^{-1} for twenty seconds. Then the precursor film was preheated at 280 ℃ for 2 min. The CZTSSe precursor film was put into a square graphite box and selenized at 555 ℃ for 15 min in Ar gas in arapid thermal processing (RTP) chamber to form CZTSSe absorber film. Afterwards, 50–80 nm CdS buffer layer was deposited on the absorber by chemical bath deposition method. Then ITO window was sputtered on CdS by magnetron sputtering under suitable O_2/Ar ratio (O_2/Ar ≈ 2%) atmosphere. Finally, the Ag electrode (70 nm) and MgF_2 antireflection layer (100 nm) were deposited onto the ITO (The active area of each device is 0.135 cm^2).

2.3. Characterization

The morphology of CZTSSe films was obtained by SEM (SUPRA 55). Illuminated and dark *J–V* characterizations were measured by a Keithley 2400 SourceMeter and a Zolix SS150 solar simulator (100 mW cm^{-2}, 25 ℃, AM 1.5 G). Atomic force microscopy (AFM) was carried out by DimensionIcon atomic force microscopy system from BrukerInc. Capacitance–voltage (*C–V*) and drive–level capacitance profiling (DLCP) were tested by a Keithley 4200A–SCS system with JANIS cryogenic platform. Admittance characterization was obtained by using a Lakeshore 325 temperature controller and the device was cooled with liquid nitrogen. Steady state photoluminescence (PL) and time-resolve photoluminescence (TRPL) were performed using time correlated single photon counting (TCSPC) (FluoTime 300, PicoQuant Gmbh). Temperature–dependent dark *J–V* (*J–V–T*) measurement was carried out using a Lakeshore 325 temperature controller and Keithley 4200A–SCS system. External quantum efficiency (EQE) was carried out by a Zolix solar cell QE/IPCE measurement system (Solar Cell Scan 100). The reflection spectrum data were analyzed by UV–3600Plus UV–VIS–NIR (SHIMADZU) spectrophotometer.

3. Results and Discussions

The thickness of WO_3 films was set as 10, 15 and 20 nm, respectively. For clarity, CZTSSe absorbers with 0, 10, 15 and 20 nm WO_3 intermediate layer were defined as W0, W10, W15 and W20, respectively. The morphology was observed by SEM of the absorbers with different WO_3 intermediate layer thickness. For W0 absorber, the microstructures of CZTSSe films exhibited a large amount of voids (**Fig. 1**a). The introduction of WO_3 intermediate layer in CZTSSe/Mo substantially facilitated the grain growth and the film densification. The SEM measurement shows that the selenized CZTSSe absorber has a typical double–layer structure, in which the upper layer is large grain layer and the lower layer is fine grain layer (Fig. 1e–h). Fine grain layers were usually due to unwanted impurity residue of organic solvents and inadequate selenization, and it will degrade cell efficiency [20]. A thick $Mo(S,Se)_2$ is presented between absorber and back electrode, which has been observed in previous studies[21,22]. With the increase of WO_3 layer thickness, the thickness of large grain layer of CZTSSe absorber increased gradually and fine grain layer decreased. In addition, compared with W0 sample, the large voids in the middle of CZTSSe film with WO_3 layer are almost invisible. Besides, it can be clearly seen from Fig. 1(h) that the $Mo(S,Se)_2$ thickness decreases radically from 690 to 400 nm after the insertion of 20 nm WO_3 at the back interface. These results confirm that the WO_3 intermediate layer does increase the crystal size, improve the crystallization of CZTSSe and reduce the $Mo(S,Se)_2$ formation.

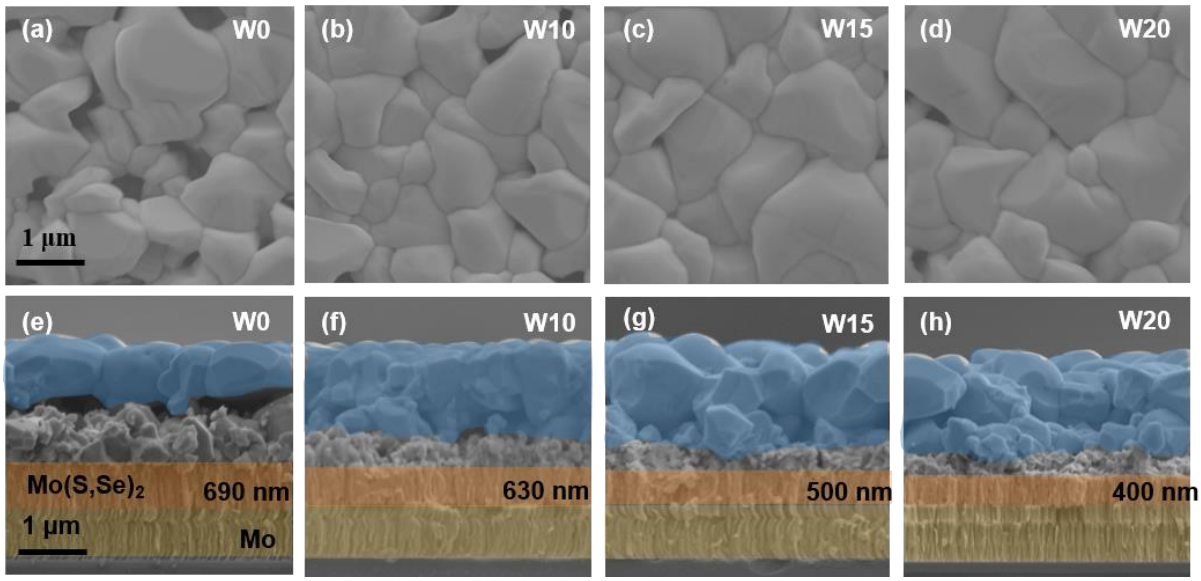

Fig. 1. Plan view (a–d) and cross–section (e–h) SEM micrographs of W0, W10, W15 and W20 CZTSSe films.

CZTSSe devices were fabricated and the effect of WO_3 intermediate layer thickness on device performance was investigated. **Fig. 2(**a) showed the conventional structure of CZTSSe solar cells with a WO_3 intermediate layer. The optimal *J–V* curves of devices with different WO_3 thicknesses are shown in Fig. 2(b), and the device parameters are listed in **Table 1**. Ten devices were constructed for each thickness to obtain statistical data. The statistic values of J_{SC}, V_{OC}, FF and PCE are shown in Fig. 2(c–f), the specific values are shown in Table 1 [23–25]. The W0 device without WO_3 achieved PCE of 10.87% with V_{OC} of 483 mV, J_{SC} of 36.2 mA cm^{-2} and FF of 62.75%. The best CZTSSe solar cell was obtained with optimized WO_3 thickness of 15 nm (W15), demonstrating a PCE of 12.66%, with V_{OC} of 524 mV, J_{SC} of 37.46 mA cm^{-2}, and FF of 65.12%. When WO_3 layer (W20) was too thick, the average performance was decreased (11.54%), which is probably because the WO_3 intermediate layer was too thick to form good back interface contact. The ideality factor (*A*) and reverse saturation current density (J_0) values of W15 device were the lowest, indicating the lower recombination of depletion region and absorber, and the improved heterojunction quality [5,26]. Besides, compared with the W0, the W15 showed lager shunt resistance (R_{sh}) and small series resistance

(R_s) (Table 1), which contributed to the increased FF [27,28]. In this work, the only difference for W0 and with W15 device was the existence of WO_3 intermediate layer, while other film preparation and device fabrication process were the same. Therefore, the improvement must be due to the optimization of the back interface.

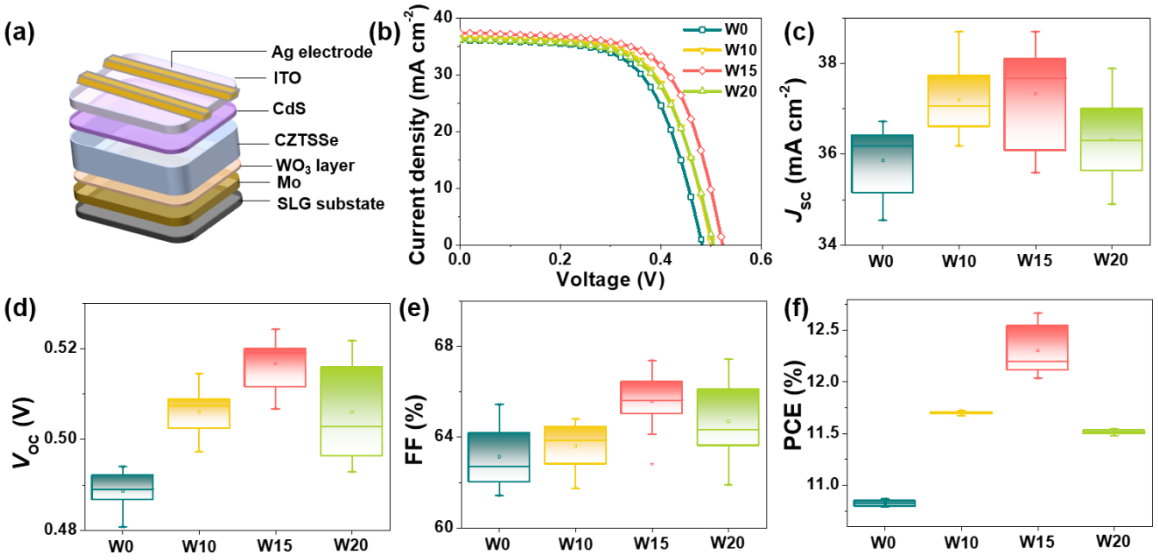

Fig. 2. (a) Structure of CZTSSe devices with WO_3 intermediate layer. (b) The *J*–*V* curves of the W0–W20 devices. Statistical box diagrams of photovoltaic parameters of Device W0–W20: (c)J_{SC}, (d)V_{OC}, (e)FF, (f)PCE. Ten cells were selected for each sample for analysis.

Table 1. Devices parameters of W0–W20.

	J_{SC} (mA cm^{-2})	V_{OC} (mV)	FF (%)	PCE (%)	J_0 (mA cm^{-2})	A	R_s (Ω•cm^2)	R_{sh} (Ω•cm^2)	V_{OC-def}
W0	36.20 (35.85 ±1.31)	0.483 (0.488 ±0.08)	62.75 (63.12 ±2.32)	10.87 (10.82 ±0.04)	6.58×10^{-3}	2.96	1.13	638	0.422
W10	36.49 (37.19 ±1.49)	0.502 (0.506 ±0.09)	64.44 (63.60 ±1.86)	11.73 (11.69 ±0.03)	2.22×10^{-4}	1.83	1.02	862	0.403
W15	37.46	0.524	65.12	12.66	7.23×10^{-5}	1.72	0.70	1030	0.381

	(37.32 ±1.72)	(0.516 ±0.010)	(65.57 ±2.76)	(12.30 ±0.36)					
W20	36.24 (36.31 ±1.56)	0.505 (0.506 ±0.016)	63.57 (64.68 ±4.78)	11.54 (11.51 ±0.03)	1.19×10^{-3}	1.93	1.05	777	0.385

To explore the WO_3 layer function on the reaction path and the grain growth mechanism of CZTSSe, W0 and W15 precursor films were selenized with different selenization time (0 s/300 s/600 s/900 s) and characterized by SEM, as shown in **Fig. 3**. Films with different selenization time were labeled as WX_t to simplify the details, where X is the thickness of WO_3, *t* indicates the selenization holding time. For example, $W15_{300}$ stands for W15 film underwent selenization for 300 s. The precursor films of W0 and W15 show similar amorphous structures (Fig. 3a $W0_0$, Fig. 3b $W15_0$). When the W0 film selenized at 555 ℃ for 300 s, larger grains appear at both the surface of the film and back interface and grow bilaterally (identified as blue crystal of $W0_{300}$ in Fig. 3c). Fig. 3(a) shows the presence of crystals on the film surface accompanied by numerous voids when the W0 film selenized at 555 ℃ for 300 s. As the selenization time is prolonged, the grain size gradually increases and crystal grows from both the top and bottom of CZTSSe film simultaneously ($W0_{600}$ in Fig. 3a). SEM images show that the thin film has a typical double–layer structure. Once the two layers come into contact, the competition for maturity begins. It is obvious that the fine grain layer at the bottom can be merged by the top large grain layer, but with the extension of selenization time, this merging behavior cannot continue indefinitely [12]. The direct result of compositive competition between the top and bottom layers is that the absorber has large voids with low surface coverage rate, because compositive competition greatly restricts the lateral growth of the top layer crystals (Fig. 3a $W0_{900}$). It can be seen from Fig. 3(c) ($W0_{900}$) that the thickness of the upper large grains of W0 is about 650 nm and there are lots of voids on the surface and in the middle of the absorber. In the case of W15, when the selenization time was 300s, grains appeared on the upper surface of W15 film only (Fig. 3b, $W15_{300}$). The SEM image of the cross section

proved that no nucleation reaction occurred at the back interface at this time (blue crystal of $W15_{300}$ in Fig. 3d). This indicates that the presence of WO_3 intermediate layer inhibits the grain growth at the back interface at the initial selenization stage. The crystal size increases with the extension of selenization time, and the large grain layer of W15 absorber is about 1.1 micron, and the crystals are closely bonded without obvious voids (Fig. 2d $W15_{900}$). Besides, as shown in the orange part of Fig. 3(c, and d), the $Mo(S,Se)_2$ thickness at back interface gradually increases with the extension of selenization time, while the $Mo(S,Se)_2$ thickness of W15 sample at each stage is significantly thinner than that of W0. We hypothesized that the significant improvement in the absorber crystallization and the decrease in $Mo(S,Se)_2$ were due to the presence of WO_3 intermediate layer, which inhibited the reaction between the absorber and Mo at the back interface during selenization, as shown in Fig. 3(e). The nucleation process starts from the CZTSSe surface due to the relatively high partial pressure of selenium on the surface. Besides, the small holes and cracks in the amorphous precursor film can facilitate Se penetrating the film. In the W0 case, where the precursor film is in direct contact with the Mo back electrode, reactions (1) can occur due to its negative Gibbs Energy at high temperature and high pressure during the selenization process [29]. This reaction can lead precursor film decomposes into some secondary phases [$Cu_2(S,Se)$, $Zn(S,Se)$, $Sn(S,Se)$] and the formation of $MoSe_2$ [10,13,30]. Then the $Cu_2(S,Se)$ compound reacts with $Sn(S,Se)$ to form $Cu_2Sn(S,Se)_3$; and $Cu_2Sn(S,Se)_3$ reacts with Zn(S, Se) to form $Cu_2ZnSn(S,Se)_4$. Liquid–phase Cu–SSe can lead to liquid–assisted grain growth, so the formation of $Cu_2(S,Se)$ at the back interface could induce and promote back interface crystallization [31,32]. The reactions of the above two steps are shown below [29,33].

$$Cu_2(S,Se)+Sn(S,Se)\rightarrow Cu_2Sn(S,Se)_3 \quad (2)$$

$$Cu_2Sn(S,Se)_3+Zn(S,Se)\rightarrow Cu_2ZnSn(S,Se)_4 \quad (3)$$

Hence, the W0 film initial nucleation occurs at the surface and the back interface of the absorber. With prolonged selenization time, the top and bottom crystal nucleus grow together and generate compositional competition. Compositive competition between multilayers will inevitably lead to compositional non–uniformity during grain growth. For the W15 film, nucleation starts from the CZTSSe surface in the initial stage of selenization. The Se vapor diffuses to the back interface through the small holes and cracks in the precursor film, but the WO_3 intermediate layer blocks the contact between precursor and Mo, inhibiting the progress of reaction (1). The existence of WO_3 inhibits the formation of the $Cu_2(S,Se)$, Zn(S,Se) and Sn(S,Se) at the back interface. The absence of these secondary phases, especially $Cu_2(S,Se)$, prevents reactions (2) and (3) from proceeding. The existence of WO_3 intermediate layer inhibits the grain growth at the CZTSSe/Mo interface of W15 film, the CZTSSe is formed from the top of W15 and its formation mechanism can be described as a top–to–down course. Therefore, the composition competition of double–layer grains is eased. The thickness of the upper large grain layer increases as the upper large grain layer merges with the bottom fine grain layer. With the extension of selenization time, the unidirectional crystal growth eventually forms the crystal structure with good crystallinity and compact grain arrangement. Besides, the form of $Mo(S,Se)_2$ was mainly limited by Se vapor diffusion in the absorber, which is the rate–determining step of $Mo(S,Se)_2$ layer formation [11]. The grain boundary (GB) of the absorber provides a pathway for the diffusion of selenium vapor, since GB diffusion of selenium vapor is more dominant than bulk diffusion. It is obvious that the crystallinity of W0 film is worse than that of W15 film, with more grain boundaries and holes. These grain boundaries and holes provide more favorable pathways for se vapor diffusion to the back interface, resulting in over thick $Mo(S,Se)_2$ of W0 sample.

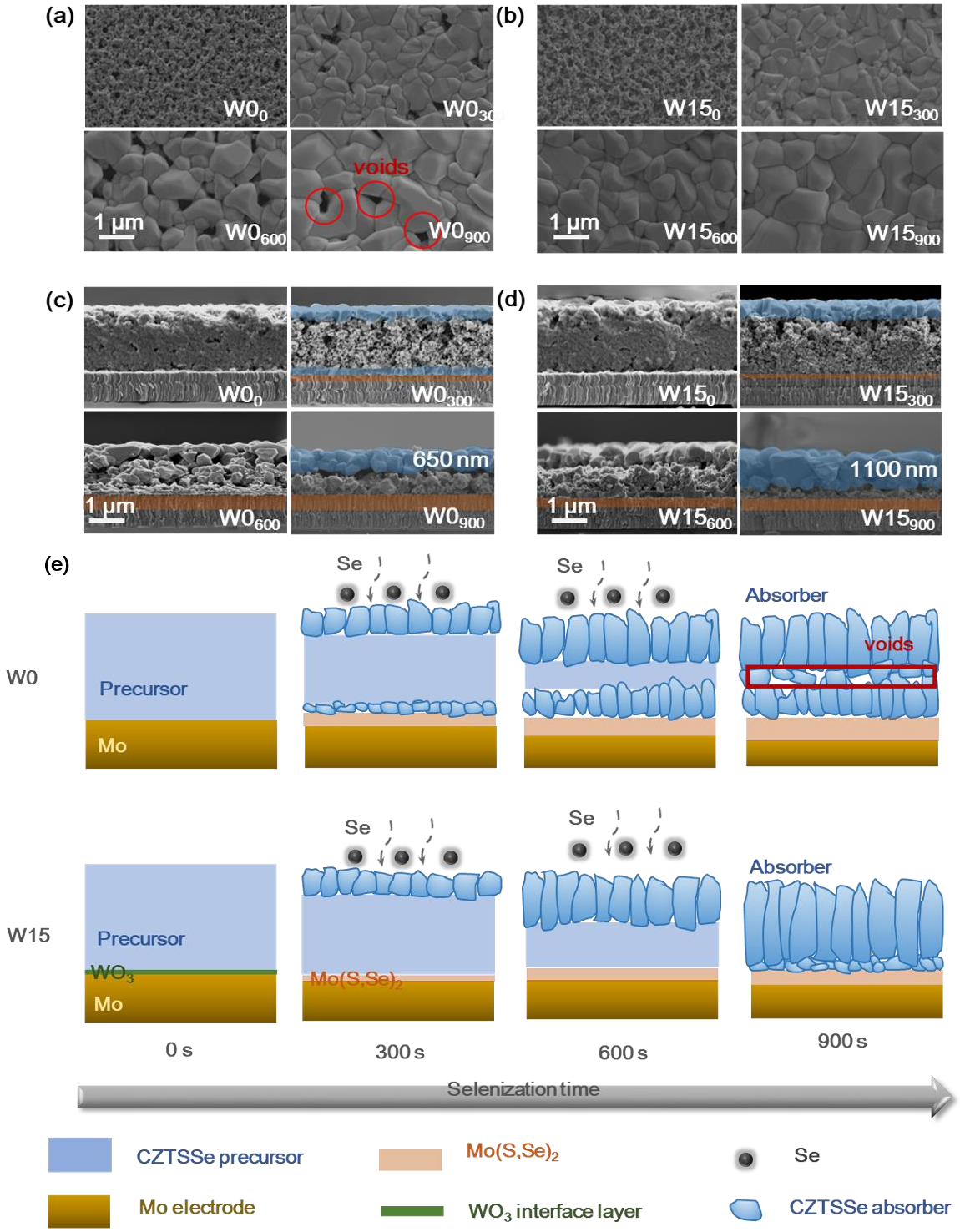

Fig. 3. Surface images (a, b) and cross–sections (c, d) SEM of W0 (a, c) and W15 (b, d) film at different selenization stage. (e) Schematic illustration of the proposed grain growth mechanism for W0 and W15 film.

The topography was further studied by AFM (**Fig. S2**). The surface of W15 film is smoother and has a smaller root–mean–square (RMS) roughness (40.2 nm) than that of the W0

film (53.0 nm). The same results were obtained by linear scanning of the surface roughness of the two films (Fig. S2c). The grain size and height distribution of W15 films were more uniform. Larger surface roughness results in incomplete coverage of CdS on the absorption, thus increasing the shunt path between window layer and absorber [6, 34]. The smooth surface of W15 film is beneficial to improving the quality of heterojunction and reducing the carriers recombination at heterojunction interface so that decrease both the dark current and interface states [35].

To evaluate the defect density of CZTSSe absorbers and recombination properties of the devices, *C–V* and DLCP measurements were conducted. The profiles obtained by *C–V* and DLCP were shown in **Fig. 4**(a) and **Table 2**. For the devices without and with WO_3 intermediate layers, the charge densities (N_{DL}, including free carriers and defects) calculated by DLCP measurement were 1.61×10^{16} cm^{-3} and 8.70×10^{15} cm^{-3} respectively. In CZTSSe, the free carriers are usually provided by shallowaccepter defects, such as V_{Cu}, which is determined mostly by the composition of CZTSSe. Therefore, the decrease in charge densities (N_{DL}) may be due to a reduction in defects with deep level, such as Cu_{Zn}, which will be discussed in detail later [36]. In addition, the profiles show that the measured depletion width of W15 device (0.192 μm) is significantly higher than that of W0 device (0.111 μm). The larger depletion width is beneficial to the collection and separation of photogenerated carriers [28]. Compared with W0 device (340 mV), the built–in potential (V_{bi}) of W15 device is increased to 561 mV (**Fig. S3**). Larger V_{bi} can form an enhanced built–in electric field, which reduces charge accumulation at the heterojunction and thus increases V_{OC} [37,38]. In general, *C–V* is more sensitive to interface defects than DLCP, CV response (N_{CV}) includes the contribution of free carriers, bulk defects and interface defects, while DLCP results (N_{DL}) only reflect the correspond of free carriers and bulk defects, thus the difference between them is the interface defect density of the device [3,39]. The interface defects density for W15 CZTSSe device (1.38×10^{15} cm^{-3}) was lower than that of W0 device (5.56×10^{15} cm^{-3}), confirming much less defective surface of W15 absorber. This

may be attributed to the fact that the absorber of W15 with improved crystallinity proved by AFM has a smoother surface, which can obtain better heterojunction quality and reduce the interface defect density. The decrease of interface defects density means that the recombination and performance degradation caused by the surface state has been suppressed.

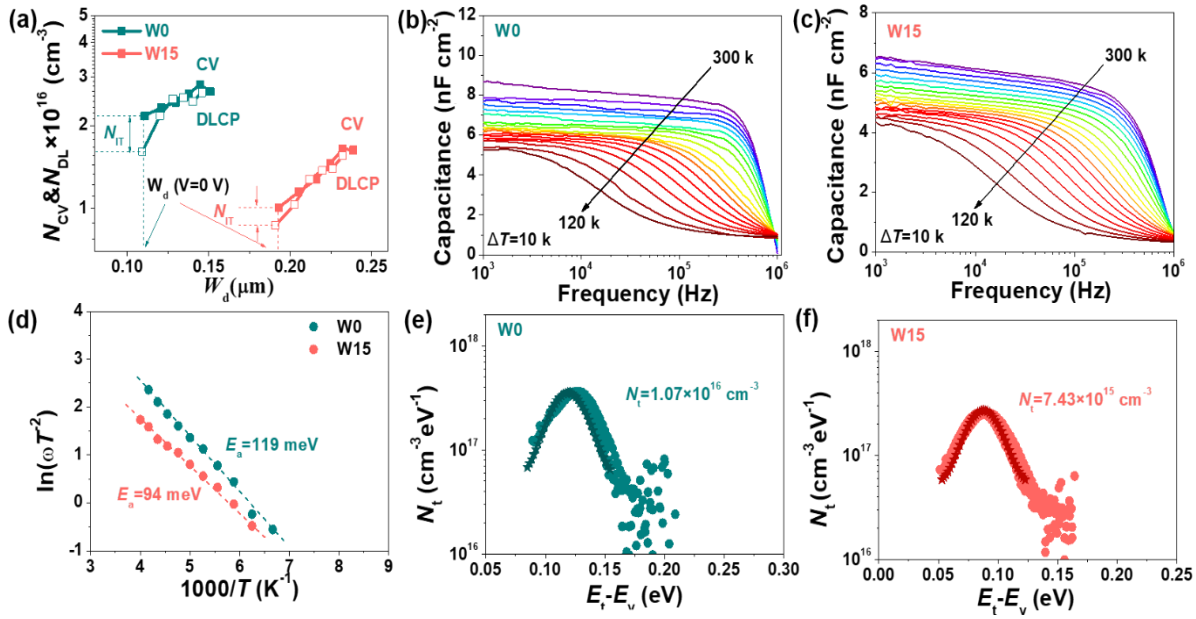

Fig. 4. (a) The profile of *C–V* and DLCP of W0 and W15 devices, Admittance spectroscopy results for (b) W0 and (c) W15 CZTSSe solar cells, the Arrhenius plots of W0 and W15 (d), the defect density of states for (e) W0 and (f) W15.

Table 2. Summary of relevant parameters of AFM, *C–V*, DLCP and TRPL measurements.

	RMS (nm)	N_{CV} (cm^{-3})	N_{DL} (cm^{-3})	Interface state response (relative values)	V_{bi} (mV)	W_d (μm)	τ (ns)	L_d (μm)
W0	53.0	2.16×10^{16}	1.61×10^{16}	5.56×10^{15}	340	0.111	0.71	0.8
W15	40.2	1.00×10^{16}	8.70×10^{15}	1.38×10^{15}	561	0.192	2.05	1.2

To further determine the defect character of CZTSSe absorber with and without WO_3 layer, AS measurements were performed on the W0 and W15 devices. The capacitance–frequency (*C–f*) spectra from 10^2 to 10^6 Hz in the temperature range of 300–120 K are shown in Fig. 4(b

and c). The high–frequency capacitance response obtained by admittance mainly caused by free carrier density, while the low–frequency capacitance represents the response caused by free carrier and deep traps [40,41]. The capacitance of W0 showed a larger variation in the low frequency region compared with W15 device (Fig. 4b and c). The capacitance of W0 device changes more obviously in the low–frequency region than that of W15 device. This significant frequency dependence of capacitance in W0 indicates higher defect density in the absorber [39] The angular frequency corresponding to the maximum of the peak in the $-f\mathrm{d}C/\mathrm{d}f$ plot yields the inflection point ω_0 [42]. We constructed an Arrhenius plot of $\ln(\omega_0/T^2)$ vs. $1000/T$ for W0 and W15 device, shown in Fig. 4(d). The Arrhenius plot was constructed using the following equation:

$$\omega_0 = 2\pi v_0 T^2 e^{-\frac{E_a}{kT}} \quad (4)$$

where E_a is the electronic state level of defect, v_0 is the emission factor [39,40]. The trap energy levels of W0 and W15 were calculated to be 119 meV and 94 meV, respectively. First–principle calculations suggest that the activation energies of the deep acceptor level of Cu_{Zn} are 100–120 meV [42,43]. The W0 defects with E_a of 119 meV and the W15 defects with E_a of 94 meV can be assigned as Cu_{Zn}. The W15 device has a lower E_a value, which means a higher hole emissivity and a lower effective recombination center concentration [28]. Therefore, the WO_3 intermediate layer between Mo and CZTSSe could suppress carrier recombination effectively.

The defect spectra are shown in Fig. 4(e and f). The calculation formula was as follows:

$$E_{(\omega)} = kTln(\frac{2\pi v_0 T^2}{\omega}) \quad (5)$$

$$N_t(E_{(\omega)}) = -\frac{V_{bi}}{W_d} \cdot \frac{dC}{d\omega} \cdot \frac{\omega}{kT} \quad (6)$$

The line composed of pentagons is a Gaussian fit of the corresponding defect energy levels [40]. Notably, the N_t of Cu_{Zn} (N_t =7.43×10^{15} cm^{-3}) in W15 is lower than the N_t of Cu_{Zn} (N_t=1.07 ×10^{16} cm^{-3}) defects in W0, which contributes to the low free carrier density. This is consistent with the decreased charge density from *C–V* and DLCP measurement. Lower and shallower

acceptor defects could effectively reduce the non–radiative recombination of the interface by reducing the carrier density of the absorber and increasing the interface hole lifetime [44,45]. In brief, the reduced N_t and E_a of acceptor defects induced by the introduction of WO_3 intermediate layer at CZTSSe/Mo interface may significantly improve the carrier collection efficiency and may also greatly contribute to the increase of V_{OC} by reducing non–radiative interface recombination. The decrease of both defect activation energy and defect density revealing the great advantage of the transition from double layer to single layer formation mechanism in fabricating high quality kesterite–based material.

To further clarify the low FF associated with the high R_s we measured the *J–V–T*. *J–V–T* plots were measured in 180–300 K in dark condition for devices without and with WO_3 intermediate layer. The devices R_s and back contact diode barrier heights can be estimated from the *J–V–T* [46,47]. In **Fig. 5**(c), from 300 to 180 K, R_s of W0 increased as much as 4 times, while R_s of W15 increased only 2 times. The existence of the blocking contact barrier Φ_B at the back interface may be one of the reasons for the divergent behavior of series resistance at low temperature. This barrier may occurr at the CZTSSe and Mo interfaces and suppress the transport of majority carrier holes. At lower temperature, the back contact diode term will dominate, by replotting the data as $\ln(R_sT)$ versus $1/T$ (Fig. 5d), compared with W0 (265 meV), W15 has a lower Φ_B (94 meV), suggesting a small barrier in W15 device, which may be related to the thin $Mo(S,Se)_2$. Obviously, W0 device showed a higher barrier and therefore had larger series resistance compared to W15 device. The exist of this Schottky barrier results in the crossover behavior of the light and dark *J–V* curves besides double diode performance (Fig. 5e) [48]. This crossover behavior occurs at lower current of the W0 device, corresponding to the higher barrier height in the device. In conclusion, the WO_3 intermediate layer significantly reduces $Mo(S,Se)_2$ thickness and the height of contact barrier in the back contact region, and ultimately improves the transport of holes in CZTSSe devices.

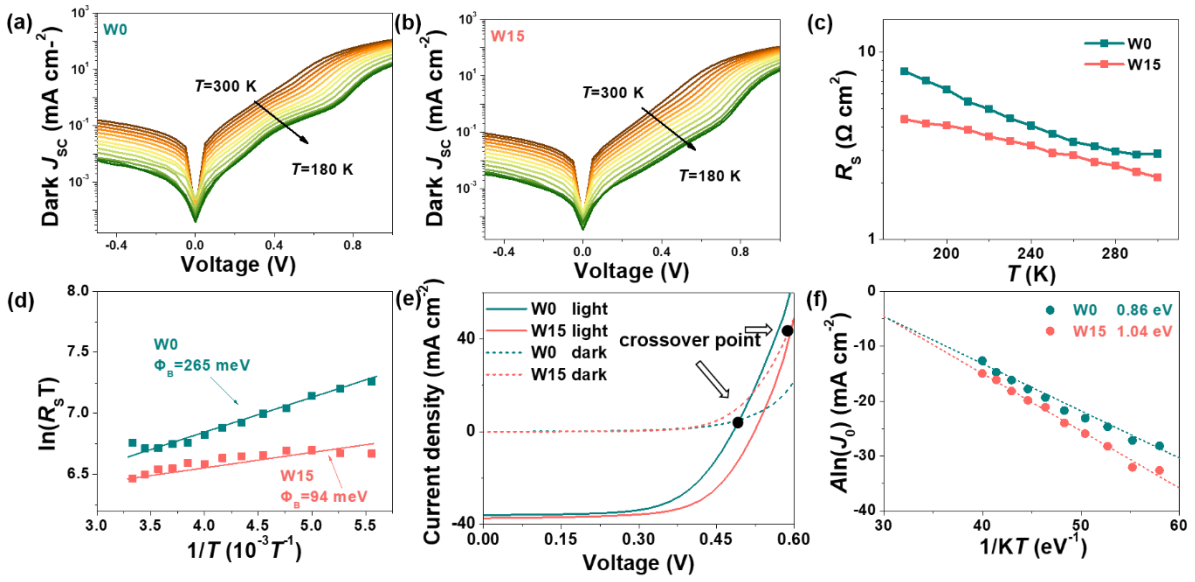

Fig. 5. *J–V–T* plots of (a) W0 device and (b) W15 device; (c) R_s–*T* curves. (d) ln(R_sT) vs 1/*T* plot for back contact barrier height determination. (e) *J–V* curves of device under light and dark state. (f) *A*ln(J_0) vs 1/k*T* plot of W0 and W15 CZTSSe devices.

In addition, *J–V–T* measurement is one of the most useful methods to determine the main composite paths in CZTSSe devices by plotting the relationship between *A*ln(J_0) and 1/k*T*, as shown in Fig. 5(f) [47]. The *A*ln(J_0) versus 1/k*T* data should yield a straight line and extrapolate to activation energy of interface recombination (E_A) at the temperature of 0 K. The estimated E_A for the W0 device is 0.86 eV while that for the W15 device is 1.04 eV. The E_g of CZTSSe films is 1.15 eV for both W0 and W15 cases which determined by the EQE analysis (**Fig. S4**). The E_A value of W0 was significantly lower than E_g, indicating that the recombination mechanism of W0 was greatly affected by interface recombination, which also limited V_{OC} at room temperature. The E_A value of W15 was close to E_g, indicating that the introduction of WO_3 intermediate layer could passivate the interface recombination significantly, which is attributed to better P–N junction quality and lower back contact barrier.

Further, to investigate the charge carrier recombination behavior and charge carrier dynamics in CZTSSe films, PL and TRPL were conducted in **Fig. S5(**a) and (b), respectively. The PL signal of W15 device is significantly increased due to the decrease of non–radiative

recombination, which further promotes the increase of V_{OC} of W15 device [49]. The decay time measured by TRPL of W15 device (2.05 ns) is much larger than that of W0 device (0.71 ns). The prolongation of carrier lifetime also indicates that WO_3 layer can significantly inhibit the non–radiative recombination of CZTSSe films, which may be related to improved crystallinity and decreased trap density of CZTSSe films [42].

The EQE and reflection (*R*) spectra of W0 and W15 sample are shown in **Fig. 6(**a and b). It can be seen that in the long wavelength range, the EQE response of W15 device reflects better carrier collection efficiency than that of W0 device, confirming higher J_{SC} [50]. This improvement can be related to better crystal quality, longer carrier lifetime and decreased $Mo(S,Se)_2$ thickness, which also contribute to FF improvement. WO_3 intermediate layer reduces $Mo(S,Se)_2$ thickness and voids in W15 absorber, thus the recombination of back interface is reduced and the carrier collection ability is improved. The E_g was determined by plotting d(–ln(1–EQE)) vs. d*E* (Fig. S3) [51,52]. E_g of W0 and W15 sample was 1.15 eV, and the presence of WO_3 layer does not change the band gap. In addition, the calculated J_{SC} from EQE were 35.04 and 36.14 mA cm^{-2}, which was in good agreement with the *J*–*V* results.

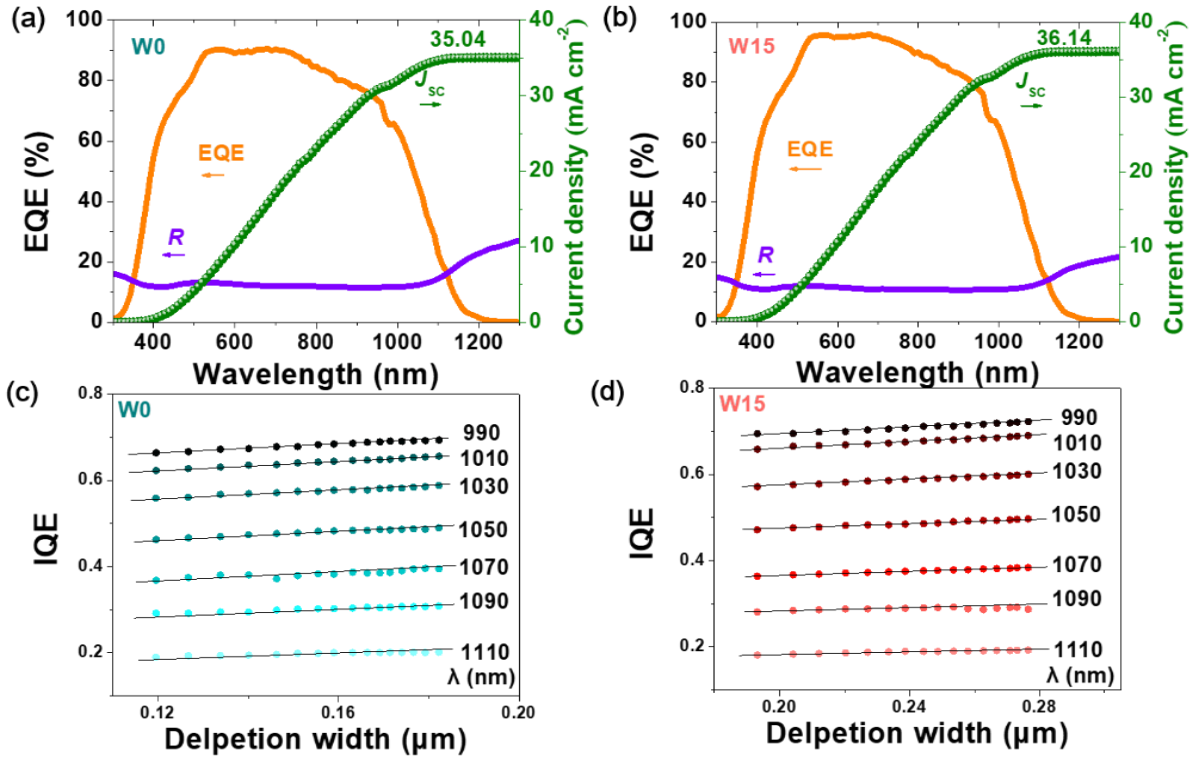

Fig. 6. EQE (orange curve) and reflection (*R*, violet curve) spectra of the W0 device (a) and W15 device (b), the green curve is the EQE integrated current, IQE at different W_d (voltage biases) and at different wavelengths near the band edge for (c) W0 and (d) W15.

We have performed minority carrier diffusion length (L_d) measurement by the bias–dependent EQE (**Fig. S6**), *C–V* (**Fig. S7**), and reflectance measurements [53,54]. The calculation formula was as follows:

$$\mathrm{IQE}(\lambda, \mathrm{V}) = \frac{\mathrm{EQE}(\lambda,\mathrm{V})}{1-\mathrm{R}(\lambda)} \qquad (7)$$

where EQE(λ,V) is measured as function of wavelength (λ) and voltage bias (V), $R(\lambda)$ is determined by the reflectivity as function of wavelength, $W_d(V)$ (the voltage dependence of the W_d) is deduced from the separate *C–V* measurement (**Fig. S8**). Then using the $W_d(V)$, the W_d dependence of IQE at each λ is obtained [IQE(λ,V)→IQE(λ,W_d)]. The array of IQE(λ,W_d) data fits into the analytical expression given by Eq.(8) to extract the L_d and the absorption coefficient (α) at each λ:

$$\mathrm{IQE}(\lambda, W_\mathrm{d}) = 1 - \frac{\exp(-\alpha(\lambda)W_\mathrm{d})}{1+\alpha(\lambda)L_\mathrm{d}} \qquad (8)$$

Fig. 6(c and d) shows the internal quantum efficiency (IQE) versus W_d at various wavelengths. When the value of IQE changes between 0.2 and 0.8, the dependence of IQE on W_d is most obvious, as shown in Fig. 6(c and d) for both samples. The minority carrier diffusion length of absorber estimated from the Fig. 6(c and d) were 0.8 μm for W0 and 1.2 μm for W15, and this may be one of the reasons for the increase of V_{OC}. The fine grain layer obstructs charge transport in the absorber, and defects provide various pathways of charge recombination at GB, on the surfaces and/or in the interface between these layers. Therefore, the thinning of fine grain layer is beneficial to the increase of carrier diffusion length. Besides, the calculation results show that the exist of WO_3 intermediate layer increases the minority carrier diffusion length from 0.8 to 1.2 μm, which is consistent with the SEM measurement showing that the thickness of large grain layer increases from 650 to 1100 nm. The results show that the W15 device has better carrier collection efficiency. Moreover, the back interface recombination is highly dependent on the carrier diffusion length, the increase of minority carrier diffusion length is beneficial to reducing back interface recombination [55].

Fig. 7 illustrates the energy band alignment and cross–section schematic diagram for W0 and W15 devices. Apparently the WO_3 intermediate layer inhibits the unfavorable interface reaction between CZTSSe and Mo in the initial stage of selenization, and high quality crystals and better interface contact are obtained. The improved crystallization could help to improve the heterojunction quality and maximize the minority carrier diffusion length, and the thin $Mo(S,Se)_2$ layer could reduce the width of the Schottky barrier and carriers can be transported more easily by the tunneling effect, which was believed to promote the CZTSSe device performance.

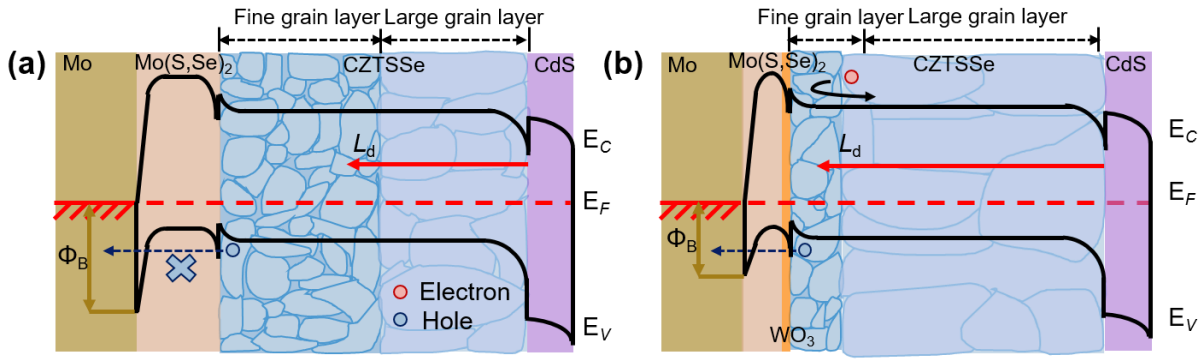

Fig. 7. The band diagrams of (a) W0 and (b) W15 CZTSSe devices.

4. Conclusions

In summary, we systematically improved the CZTSSe device performance by introducing WO_3 intermediate layer to optimize the crystal growth process. WO_3 intermediate layer successfully inhibited the adverse reaction between Mo and CZTSSe, which resulted in poor crystallinity and thick $Mo(S,Se)_2$ layer. And finally, high quality CZTSSe crystal with low defect density and good charge transfer ability was obtained, and the smooth absorber surface also improved the quality of P–N junction. Besides, the inhibition of the back interface reaction effectively decreased the thickness of $Mo(S,Se)_2$, lowered the back interface contact barrier and significantly boosted the fill factor. The introduction of WO_3 intermediate layer not only improved the minority carrier diffusion length, but also decreased the deep accepter defects, which greatly inhibited the non–radiative recombination of devices and thus decreased the open circuit voltage deficit. As a result, we demonstrated efficiency improvement from 10.87% to 12.66% in CZTSSe solar cell with a pronounced increase in V_{OC} and FF and a slight increase in J_{SC}. Our work provided an effective pathway to regulate selenization process and crystal growth by introducing WO_3 intermediate layer as isolation layer for highly efficient CZTSSe solar cells.

Declaration of Competing Interest

The authors declare that they have no known competing financial interests or personal relationships that could have appeared to influence the work reported in this paper.

Acknowledgments

This work was supported by the National Natural Science Foundation of China (no. 62074102), the Key Project of Department of Education of Guangdong Province (no. 2018KZDXM059), and the Science and Technology plan project of Shenzhen (nos. JCYJ20190808153409238, JCYJ20190808120001755, 20200826143347001 and 20220808165025003).

References

[1] Y. Sun, P. Qiu, W. Yu, J. Li, H. Guo, L. Wu, H. Luo, R. Meng, Y. Zhang, S. F. Liu, Adv. Mater. 33 (2021) e2104330.

[2] M. He, C. Yan, J. Li, M.–P. Suryawanshi, J. Kim, M.–A. Green, X. Hao, Adv. Sci. 8 (2021) 2004313.

[3] Z. Su, G. Liang, P. Fan, J. Luo, Z. Zheng, Z. Xie, W. Wang, S. Chen, J. Hu, Y. Wei, C. Yan, J. Huang, X. Hao, F. Liu, Adv. Mater. 32 (2020) e2000121.

[4] M.–A. Green, E.–D. Dunlop, J. Hohl‐Ebinger, M. Yoshita, N. Kopidakis, K. Bothe, D. Hinken, M. Rauer, X. Hao, Photovolt. Res. Appl. 30 (2022) 687–701.

[5] Y. Gong, Y. Zhang, Q. Zhu, Y. Zhou, R. Qiu, C. Niu, W. Yan, W. Huang, H. Xin, Energy Environ. Sci. 14 (2021) 2369–2380.

[6] R. Fonoll–Rubio, J. Andrade–Arvizu, J. Blanco Portals, I. Becerril, M. Guc, E. Saucedo, F. Peiro, L. Calvo–Barrio, M. Ritzer, C.–S. Schnohr, M. Placidi, S. Estrade, V. Izquierdo–Roca, A. Perez–Rodriguez, Energy Environ. Sci. 14 (2021) 507–523.

[7] H. Guo, R. Meng, G. Wang, S. Wang, L. Wu, J. Li, Z. Wang, J. Dong, X. Hao, Y. Zhang, Energy Environ. Sci. 15 (2022) 693–704.

[8] S. Giraldo, Z. Jehl, M. Placidi, V. Izquierdo–Roca, A. Perez–Rodriguez, E. Saucedo, Adv. Mater. 31 (2019) e1806692.

[9] C. Yan, J. Huang, K. Sun, S. Johnston, Y. Zhang, H. Sun, A. Pu, M. He, F. Liu, K. Eder, L. Yang, J.–M. Cairney, N. J. Ekins–Daukes, Z. Hameiri, J.–A. Stride, S. Chen, M.–A. Green, X. Hao, Nat. Energy 3 (2018) 764–772.

[10] J.–J. Scragg, J.–T. Watjen, M. Edoff, T. Ericson, T. Kubart, C. Platzer–Bjorkman, J. Am. Chem. Soc. 134 (2012) 19330–19333.

[11] V. Karade, A. Lokhande, P. Babar, M.–G. Gang, M. Suryawanshi, P. Patil, J.–H. Kim, Sol. Energy Mater. Sol. Cells 200 (2019) 109911.

[12] Q. Yu, J. Shi, L. Guo, B. Duan, Y. Luo, H. Wu, D. Li, Q. Meng, Nano Energy 76 (2020) 105042.

[13] S. López–Marino, M. Placidi, A. Pérez–Tomás, J. Llobet, V. Izquierdo–Roca, X. Fontané, A. Fairbrother, M. Espíndola–Rodríguez, D. Sylla, A. Pérez–Rodríguez, E. Saucedo, J. Mater. Chem. A 1 (2013) 8338.

[14] F. Liu, J. Huang, K. Sun, C. Yan, Y. Shen, J. Park, A. Pu, F. Zhou, X. Liu, J. A. Stride, M.–A. Green, X. Hao, NPG Asia Mater. 9 (2017) e401.

[15] G.–X. Liang, Z.–X. Yu, Z.–G. Xie, Y. He, J.–H. Lin, S. Chen, Z.–H. Zheng, J.–T. Luo, P. Fan, Z.–H. Su, H.–L. Ma, X.–H. Zhang, Solar RRL 5 (2021) 2100574.

[16] J. Fu, D. Kou, W. Zhou, Z. Zhou, S. Yuan, Y. Qi, S. Wu, J. Mater. Chem. A 8 (2020) 22292–22301.

[17] H. Cui, X. Liu, F. Liu, X. Hao, N. Song, C. Yan, Appl. Phys. Lett. 104 (2014) 041115.

[18] B. Shin, Y. Zhu, N. A. Bojarczuk, S. Jay Chey, S. Guha, Appl. Phys. Lett. 101 (2012) 053903.

[19] K. Shi, B. Yao, Y. Li, Z. Ding, R. Deng, Y. Sui, Z. Zhang, H. Zhao, L. Zhang, Superlattices Microstruct. 113 (2018) 328–336.

[20] Y. Du, Q. Tian, J. Huang, Y. Zhao, X. Chang, A. Zhang, S. Wu, Sustainable Energy Fuels 4 (2020) 1621–1629.

[21] P. Fan, Z. Xie, G. Liang, M. Ishaq, S. Chen, Z. Zheng, C. Yan, J. Huang, X. Hao, Y. Zhang, Z. Su, J. Energy Chem. 22 (2021) 186–194.

[22] Y. Deng, Z. Zhou, X. Zhang, L. Cao, W. Zhou, D. Kou, Y. Qi, S. Yuan, Z. Zheng, S. Wu, J. Energy Chem. 61 (2021) 1–7.

[23] Z. Shen, S. Wang, Y. Liu, Y. Sun, J. Wu, H. Guo, K. Zhang, S. Zhang, F. Liu, Y. Zhang, J. Energy Chem. 27 (2021) 637–644.

[24] J. R. Sites, Sol. Energy Mater. Sol. Cells 75 (2003) 243–251.

[25] D. Wang, J. Wu, X. Liu, L. Wu, J. Ao, W. Liu, Y. Sun, Y. Zhang, J. Energy Chem. 12 (2019) 188–196.

[26] Y.–H. Zhao, Q.–Q. Gao, S.–J. Yuan, Q.–Q. Chang, T. Liang, Z.–H. Su, H.–L. Ma, S. Chen, G.–X. Liang, P. Fan, X.–H. Zhang, S.–X. Wu, Chem. Eng. J. 436 (2022) 135008.

[27] S. Yuan, X. Wang, Y. Zhao, Q. Chang, Z. Xu, J. Kong, S. Wu, ACS Appl. Energy Mater. 3 (2020) 6785–6792.

[28] Y. Zhao, S. Yuan, Q. Chang, Z. Zhou, D. Kou, W. Zhou, Y. Qi, S. Wu, Adv. Funct. Mater. 31 (2020) 2007928.

[29] J. Li, Y. Zhang, H. Wang, L. Wu, J. Wang, W. Liu, Z. Zhou, Q. He, Y. Sun, Sol. Energy Mater. Sol. Cells 132 (2015) 363–371.

[30] F. Liu, F. Zeng, N. Song, L. Jiang, Z. Han, Z. Su, C. Yan, X. Wen, X. Hao, Y. Liu, ACS Appl. Mater. Interfaces 7 (2015) 14367–14383.

[31] J.–F. Guillemoles, P. Cowache, A. Lusson, K. Fezzaa, F. Boisivon, J. Vedel, D. Lincot, J. Appl. Phys. 79 (1996) 7293–7302.

[32] S.–Y. Kim, D.–H. Son, S.–H. Kim, Y.–I. Kim, S. Kim, K. Ahn, K.–J. Yang, J.–K. Kang, D.–H. Kim, Adv. Energy Mater. 10 (2020) 1903173.

[33] A. Fairbrother, X. Fontané, V. Izquierdo–Roca, M. Espíndola–Rodríguez, S. López–Marino, M. Placidi, L. Calvo–Barrio, A. Pérez–Rodríguez, E. Saucedo, Sol. Energy Mater. Sol. Cells 112 (2013) 97–105.

[34] Y. Sun, H. Guo, P. Qiu, S. Zhang, S. Wang, L. Wu, J. Ao, Y. Zhang, J. Energy Chem. 10 (2020) 618–626.

[35] P. Fan, Y. He, G. Liang, Z. Xie, Z. Yu, J. Lin, S. Chen, Z. Zheng, J. Luo, Z. Su, J. Mater. Chem. A 534 (2021) 25196–25207.

[36] S. Chen, A. Walsh, X. G. Gong, S. H. Wei, Adv. Mater. 25 (2013) 1539.

[37] J. Li, D. Wang, X. Li, Y. Zeng, Y. Zhang, Adv. Sci. 5 (2018) 1700744.

[38] B. Ohnesorge, R. Weigand, G. Bacher, A. Forchel, W. Riedl, Appl. Phys. Lett. 73 (1998) 1224.

[39] H.–S. Duan, W. Yang, B. Bob, C.–J. Hsu, B. Lei, Y. Yang, Adv. Funct. Mater. 23 (2013) 1471.

[40] Y.–D. Luo, R. Tang, S. Chen, J.–G. Hu, Y.–K. Liu, Y.–F. Li, X.–S. Liu, Z.–H. Zheng, Z.–H. Su, X.–F. Ma, P. Fan, X.–H. Zhang, H.–L. Ma, Z.–G. Chen, G.–X. Liang, Chem. Eng. J. 393 (2020) 124599.

[41] R. Tang, Z.–H. Zheng, Z.–H. Su, X.–J. Li, Y.–D. Wei, X.–H. Zhang, Y.–Q. Fu, J.–T. Luo, P. Fan, G.–X. Liang, Nano Energy 4 (2019) 103929.

[42] J. Li, Y. Huang, J. Huang, G. Liang, Y. Zhang, G. Rey, F. Guo, Z. Su, H. Zhu, L. Cai, K. Sun, Y. Sun, F. Liu, S. Chen, X. Hao, Y. Mai, M.–A. Green, Adv. Mater. 32 (2020) 2005268.

[43] K.–J. Yang, J.–H. Sim, B. Jeon, D.–H. Son, D.–H. Kim, S.–J. Sung, D.–K. Hwang, S. Song, D.–B. Khadka, J. Kim, J.–K. Kang, Prog. Photovolt. 23 (2015) 862–873.

[44] J. Li, S. Kim, D. Nam, X. Liu, J. Kim, H. Cheong, W. Liu, H. Li, Y. Sun, Y. Zhang, Sol. Energy Mater. Sol. Cells 159 (2017) 447–455.

[45] J. Li, J. Huang, Y. Huang, H. Tampo, T. Sakurai, C. Chen, K. Sun, C. Yan, X. Cui, Y. Mai, X. Hao, Solar RRL 5 (2021) 2100418.

[46] O. Gunawan, T.–K. Todorov, D.–B. Mitzi, Appl. Phys. Lett. 97 (2010) 233506.

[47] G.–S. Park, V.–B. Chu, B.–W. Kim, D.–W. Kim, H.–S. Oh, Y.–J. Hwang, B.–K. Min, ACS Appl. Mater. Interfaces 10 (2018) 9894–9899.

[48] D. Cozza, C.–M. Ruiz, D. Duché, J.–J. Simon, L. Escoubas, IEEE J. Photovolt. 6 (2016) 1292–1297.

[49] J.–M. Marin‐Beloqui, D. T. W. Toolan, N.–A. Panjwani, S. Limbu, J.–S. Kim, T.–M. Clarke, Adv. Energy Mater. 11 (2021) 2100539.

[50] Y. Zhao, S. Yuan, D. Kou, Z. Zhou, X. Wang, H. Xiao, Y. Deng, C. Cui, Q. Chang, S. Wu, ACS Appl. Mater. Interfaces 12 (2020) 12717–12726.

[51] J. Mattheis, U. Rau, J.–H. Werner, J. Appl. Phys. 101 (2007) 113519.

[52] S. Hadke, S. Levcenko, G. Sai Gautam, C.–J. Hages, J.–A. Márquez, V. Izquierdo-Roca, E.–A. Carter, T. Unold, L.–H. Wong, Adv. Energy Mater. 9 (2019) 1902509.

[53] Y. Lee , T. Gershon , O. Gunawan, T.–K. Todorov , T. Gokmen , Y. Virgus, S. Guha, Adv. Energy Mater. 5 (2015) 1401372.

[54] T. Gokmen, O. Gunawan, D.–B. Mitzi, J. Appl. Phys. 114 (2013) 114511.

[55] M. Ochoa, S. Buecheler, A.–N. Tiwari, R. Carron, Energy Environ. Sci. 13 (2020) 2047–2055.

Graphical abstract

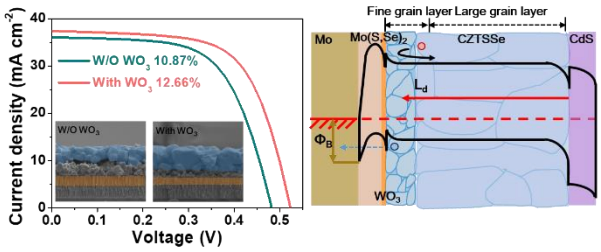

The effects of WO_3 intermediate layer on the microstructure, electrical and defects properties of CZTSSe films is revealed for the first time, high quality CZTSSe crystal and low back interface contact barrier is obtained.